Accurate Quantification of Small Pulmonary Nodules Using 3D Reconstruction of 2D Computed Tomography Lung Images

Ayat Karrar[1], Mai S. Mabrouk[2], Manal Abdel Wahed[3]

[1] Systems and Biomedical Engineering, Cairo University, Giza, Egypt, ytkarrar @yahoo.com

[2] Biomedical Engineering, Misr University for Science and Technology (MUST), 6th of October, Egypt, Msm_eng@yahoo.com

[3] Systems and Biomedical Engineering, Cairo University, Giza, Egypt,

Corresponding author(s) E-mail: Manal.wahed@eng1.cu.edu.egy

ABSTRACT

Lung cancer has a high incidence rate and is considered highly fatal because of its low survival rate at early stages compared to other cancers. Computed tomography (CT) scans can reveal pulmonary nodules of different shapes and volumes in two dimensional (2D) slices. Three-dimensional (3D) reconstruction of pulmonary nodules can assist the radiologist in early treatment appropriate for the 3D nodule volume screened. In this research, we present a 3D reconstruction algorithm that uses 2D CT slices to reconstruct a 3D lung nodule. The equivalent diameters of small nodules ranged from 3 to 30 mm. A segmentation approach (based on bounding boxes and maximum intensity projection) was applied. Extracting the lung nodules from the 2D candidate masses was performed via a rule-based classifier. Surface rendering was used to reconstruct 3D pulmonary nodules which were visualized on the 3D Slicer software. The 3D nodule volume, as well as the accuracy rate and error of volume estimation were calculated. The proposed methodology was validated against the actual volumes of 14 3D nodules from the Lung Image Database Consortium (LIDC) database. The proposed algorithm achieved a maximum accuracy of 99.6627 % for lung nodule volume estimation. The corresponding average accuracy rate and average percentage error were 97.34 % and 2.66 %, respectively. The screening of 3D lung nodules can support surgery planning via nodule volume estimation. The average accuracy and error rates of the 3D reconstruction algorithm showed promising results in comparison with other published studies.

1. INTRODUCTION

Lung cancer has been identified as the leading cause of death worldwide [1]. Its symptoms are typically manifested at an advanced stage, and this makes effective treatment difficult. The overall 5-year survival rate following early-stage lung cancer detection is approximately 54 %, whereas the rate for advanced-stage detection is only 4% [2]. Thus, early lung nodule detection and diagnosis are critical to increase the life expectancy of patients. Studies by Field et al. [3] and Scholten et al. [4] showed that computed tomography (CT) has greater sensitivity for nodule detection than that of traditional X-ray-based screening and is frequently used for lung cancer detection and diagnosis. Indeed, micronodules do not always appear on a two-dimensional (2D) CT slice as their high complexity impairs the ability to distinguish between micronodules and blood vessels. Therefore, lung nodule segmentation is a critical step in differentiating between the micronodules and other masses in CT slices. A perfect three-dimensional (3D) reconstruction requires highly accurate 2D nodule segmentation. Volumetric assessment of 3D reconstructed nodules is a key parameter to measure

the nodule response to therapy. Indeed, lesion volume estimation gives a brief indication of the area occupied by lesion tissues and in turn can help radiologists plan the treatment accordingly [5]. For instance, Diego et al. [6] proposed a lung cancer detection method involving steps of a 2D algorithm for preprocessing and enhancement, a 3D blob algorithm for 3D blob segmentation, and a support vector machine (SVM) classifier. Ramyasri et al. [5] presented a K-means algorithm for lesion volume estimation. The results of this algorithm were validated with the 3D Slicer software, and the volume estimation errors for the solid and non-solid lesion portions were determined to be between 1.11% to 3.30% and 0.1% to 4.55%, respectively.

Jinke et al. [7] proposed a lung segmentation scheme consisting of three phases: skin boundary detection, parenchyma refinement, and lung contour rough segmentation. The proposed system was evaluated with 45 volumes of CT scans, based on five metrics, namely, the volume difference, the volume overlap error, the average surface distance, the root-mean-square distance, and the maximum symmetric absolute surface distance. This system achieved an average

error rate of 3.5 1%. Chen et al. [8] proposed an active contour segmentation model based on a new fuzzy speed function, whose computation is based on intensity features and a local shape index. Bin et al. [9] used an adaptive local-region energy term in the active contour model for juxta-vascular nodule segmentation. In a broader sense, all deformable models use either region-based or boundary-based image information to improve the segmentation outcomes. However, boundary-based segmentation shows poor convergence for noisy or weak boundaries. Hina et al. [1] performed nodule segmentation by incorporating a mean-intensity-based threshold in a geodesic active contour model. An adaptive technique using image intensity histogram to estimate the desired mean intensity of the nodule was also proposed. The system was validated on both lung nodules and phantoms. Quantitative and visual comparative analysis of the proposed work using the Chan-Vese algorithm and statistical active contour model of the 3D Slicer platform was also presented. Prionjit et al. [10] adopted several morphological processing techniques to remove background, noise, and airways from lung CT images. Then, K-means clustering was utilized for lung segmentation and tumor detection. Volumetric analysis of the lung nodules for the prediction of the tumor stages was performed according to the tumor nodule metastasis classification. Yang et al. [11] proposed a 3D pulmonary nodule detection system for multi-slice CT images. This system segmented the candidate nodules and extracted the features based on an analysis of the eigenvalues of a Hessian matrix. Then, SVM and decision rules divided the candidates into two classes and removed false positives. Serhat et al. [12] used a genetic cellular neural network for the segmentation step. The regions of interest (ROI) were then extracted using an eight-directional search, and +1 or −1 values were assigned to each voxel. A 3D template was used to find nodule-like structures on the 3D ROI image. Satya et al. [13] proposed a method for lung segmentation in CT images using a fuzzy c-means clustering approach with automatic thresholding and morphological operations. This achieved an average overlap ratio difference of 5.8% with average over- and under-segmentation rates of 3.9% and 1.9%, respectively. William et al. [14] described three-dimensional (3-D) methods for the segmentation, analysis, and characterization of small pulmonary nodules imaged using computed tomography (CT). Methods for the isotropic resampling of anisotropic CT data are discussed. Also, 3-D intensity and morphology-based segmentation algorithms are discussed for several classes of nodules. New models and methods for volumetric growth characterization based on longitudinal CT studies are developed. The results of segmentation and growth characterization methods based on in vivo studies are described. Stefano et al. [15] described a semiautomatic method for 3-D segmentation of lung nodules in CT images for subsequent volume assessment. The distinguishing features of the algorithm are the following: 1) The user interaction process and 2) The adoption of the geodesic distance in a multithreshold image representation. The algorithm was validated on low-dose CT scans of small nodule phantoms (mean diameter 5.3-11 mm) and in vivo lung nodules (mean diameter 5--9.8 mm) detected in the Italung-CT screening program for lung cancer. The authors observed a RMS error less than 6.6% in phantoms, and the correct outlining of the nodule contour was obtained in 82/95 lung nodules of Italung-CT and in 10/12 lung nodules of LIDC first data set. Jamshid et al. [16] presented an efficient algorithm for segmenting different types of pulmonary nodules including high and low contrast nodules. The algorithm performs an adaptive sphericity oriented contrast region growing on the fuzzy connectivity map of the object of interest. This region growing is operated within a volumetric mask which is created by first applying a local adaptive segmentation algorithm that identifies foreground and background regions within a certain window size. The foreground objects are then filled to remove any holes, and a spatial connectivity map is generated to create a 3-D mask. The mask is used to estimate the parameters for the subsequent region growing, as well as for repositioning the seed point in order to ensure reproducibility. The method was run on 815 pulmonary nodules. In this paper, a robust model is proposed for 3D reconstruction of solitary and juxtapleural lung nodules from 2D CT scans. In this model, a nodule segmentation and enhancement scheme is applied using bilateral filtering, gray-level thresholding, bounding box localization, and the maximum intensity projection algorithms. Rule-based classification was achieved with shape and texture features. Surface rendering was employed for 3D reconstruction of pulmonary nodules, which were then visualized using the 3D Slicer software via a MATLAB interface. The volumes of the reconstructed nodules were also estimated. Fig. 1 shows the main block diagram of the 3D reconstruction algorithm.

2. MATERIALS AND METHODS
A. Dataset description

In total, 14 digital DICOM-format CT images consisting of 2991 2D slices with 172 nodules (100 solitary nodules and 72 juxtapleural nodules) were obtained from the Cornell University LIDC dataset [17]. Each abnormal image contained a tumor with equivalent diameters of small lung nodules ranging from 3 to 30

mm. The in-slice *(x, y)* resolution was 0.703×0.703 mm, while each CT slice had a thickness of 1.25 mm and dimensions of 512×512 pixels.

B. Segmentation and enhancement for nodule emphasis

Inhomogeneity in the lung region is a very challenging problem as tissue structures such as veins, arteries, and bronchioles have similar densities. Therefore, it is necessary to enhance the quality of the displayed image by rectifying distortions due to media decay or motion artifacts [18]. In this work, the segmentation approach was explained in details in [18]. This approach exploits bilateral filtering [18-19], gray-level thresholding via a bit-plane slicing technique [18-20], bounding-box localization [21], and the maximum intensity projection algorithm [22].
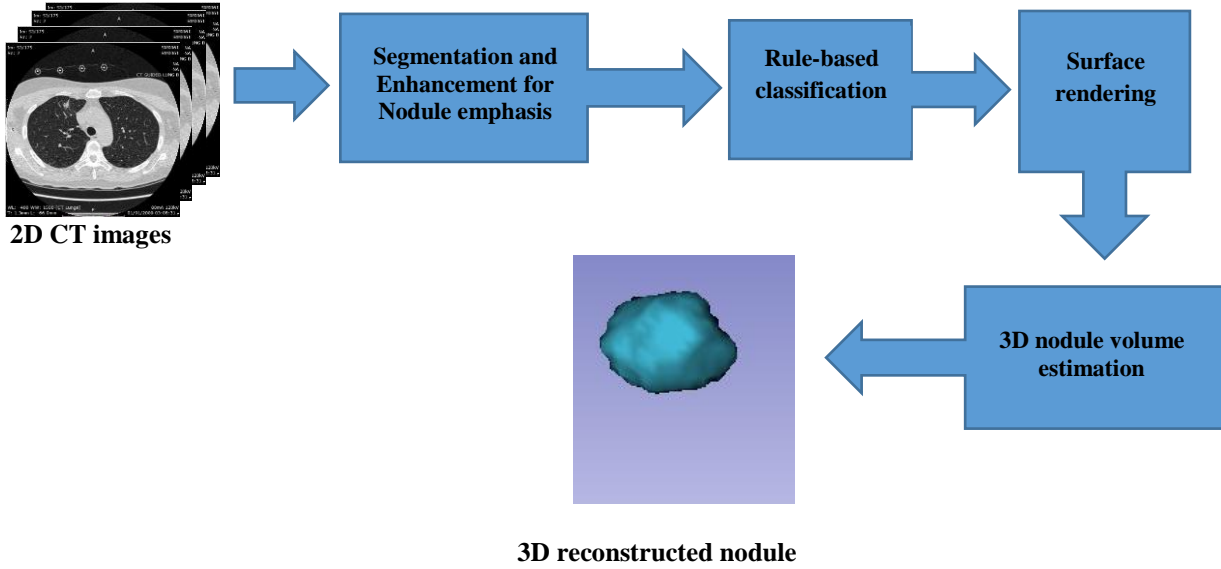

3D reconstructed nodule

Figure 1: The main block diagram of the 3D reconstruction algorithm

C. The 3D nodule reconstruction

Although a traditional chest CT scan may be appropriate for nodule detection, using a 3D model allows full operative planning [23] from port placement [24] to anatomical resection [25]. 3D reconstruction is performed to visualize the 3D tumor so that the volume can be estimated in order to assist the physician with diagnosis and surgery [26]. The 3D tumor rule-based classifier, surface rendering, and 3D Slicer were used to visualize and allocate the 3D tumors.

C.1 Rule-based classifier

A rule-based classifier was employed to reduce the large number of non-nodule candidates and extract the 2D nodules via some rules. These rules are based on four 2D shape features and one texture feature [27]. Four rules are based on shape features (namely, equivalent diameter, eccentricity, solidity, and roundness) and one rule is based on texture features (namely, the gray-level values) [28]. These rules will be explained as follows.

*1. Area and Equivalent Diameter*: Area is the total number of pixels in the region of interest. Since the equivalent diameter in our dataset ranges from 3mm to 3cm (small nodule), this feature is a pertinent one as the equivalent diameter feature determines the diameter of a circle with the same region of interest (ROI) of the object which may be a nodule in the image. Equation (1) estimates the equivalent ROI diameter.

$$\text{Equivalent Diameter} = \sqrt{4 \times Area \,/pi} \qquad (1)$$

2. Perimeter: The number of pixels in the object boundary.

3. Eccentricity: The ratio between the longest chord of a shaped object and longest chord perpendicular to it. It is a measure of how circular a shape is. The eccentricity is zero for a perfectly circular shape. For elliptical shapes, the eccentricities are between zero and one. Elongation is the ratio between the height and width for a rotated minimal bounding box.

4. Solidity: A measure of the density of an object. It is the ratio between the area of an object and the area of a convex hull of the object (Equation 2). The convex hull of an object is defined as the smallest convex shape that contains the object. A value of 1 indicates a solid object, and a value less than 1 indicates an object with an irregular boundary.

$$\text{Solidity} = \text{Area/ Convex area} \qquad (2)$$

5. *Roundness*: An indication of how round an object is:

$$\text{Roundness} = \quad (3)$$

Primary Isosurface

Reconstructed Isosurface
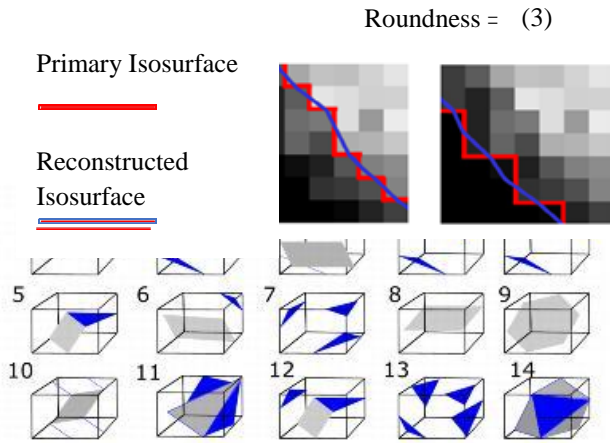
$*Area\ /\ Perimeter^2$

Roundedness is equal to one for a circle and is less than one for other shapes.

6. *Minimum and maximum gray-level values:* In general, nodules have mean gray-level values higher than those of blood vessels. Nevertheless, the gray-level values depend on the scan set resolution.

C.2 Surface rendering

Rendering techniques were used to visualize the CT data as 3D volumes. The conventional rendering techniques for medical images are multiplan rendering, surface rendering (SR), and volume rendering. In this work, the SR technique was applied [29]. This is also referred to as threshold-based rendering which is based on the marching-cube algorithm. This algorithm generates surfaces from regions with similar voxel values in the 3D data at the eight corners of a cube. The threshold can then be rendered into surfaces (Isosurface). Each surface contains points that have the same intensity (called iso-values) on all slices. The threshold is set to a specific brightness value. The isosurface marks the border between values below and above the threshold. The voxels that are intersected by the threshold value are identified. Each of the voxel 8 vertices can be either inside or outside of the isosurface value, thus, there are $2^8 = 256$ combinations. These combinations were reduced to 15 combinations as shown in fig. 2. Edge values were used to map the vertices under the isosurface to the intersecting edges. Each bit according to the isolevel returned 0 if the edge isn't cut by the isosurface and 1 if the edge is cut by the isosurface. All points of intersection in each cube were calculated by linear interpolation,

$$P = P_1 + (isovalue - V_1)(P_2 - P_1)/(V_2 - V_1) \quad (4)$$

where P is the intersection point; P_1 and P_2 are the vertices of a cut ed $\quad$ $d\ V_2$ are the scalar values of each verte $\quad$ (3) $\quad$ hm then generates a reconstruction for s $\quad$ arance as shown in fig. 3. The 3D Slicer 4.8.1 software [30] was used (in conjunction with a MATLAB interface [31]) for visualizing the 3D reconstructed nodules.

Figure 2: 256 cubes reduction to a total of 15 cubes

Figure 3: Surface rendering technique
(a) Primary and reconstructed isosurfaces for grayish ROI
(b) Primary and reconstructed isosurfaces for black ROI

C.3 Nodule volume estimation

As tumors lack well-defined regular shapes, the tumor volumes are difficult to calculate. To overcome this problem, voxel counting is used for merging the two-dimensional boundaries into a volume. The estimation of nodule volume V_E is based on the total number of voxels within the segmented region (ROI) by counting pixels on image planes and then summation of boundary area in a 3D array; in our case: x and y are the dimensions of the pixel and z is the slice thickness (depth) which form the unit voxel. Most volume measurement methods use voxel counting [32].

To estimate the nodule volume in mm^3, we should convert the estimated volume resulted from the voxel counting using the next equation (5):

Volume of nodule in $mm^3 =$
Volume of nodule in voxels * Spatial calibration factor $\quad$ (5)

Where the spatial calibration factor is (mm per pixel x, mm per pixel y, mm per pixel z)
According to our dataset, the spatial calibration factor $= 0.703 \times 0.703 \times 1.25 = 0.61$
The proposed algorithm was tested on the 14 LIDC CT samples based on the ground-truth actual tumor volumes (V_A) and the volumes (V_E) estimated by the proposed algorithm [31]. The difference volume (V_D) was measured as

$$V_D = V_E - V_A \quad (6)$$

The percentage error of the estimated lung nodule volume was calculated as

$$E\% = V_D/V_A \times 100 \quad (7)$$

The accuracy rate of the estimated lung nodule volume was calculated as

$$A_R = 100 - E\% \qquad (8)$$

The average error rate and the average accuracy rate of the proposed model were estimated respectively as [33]

$$Average\ error\ rate = \frac{1}{n}\sum_{t=1}^{n} E, \qquad (9)$$

$$Average\ accuracy\ rate = \frac{1}{n}\sum_{t=1}^{n} A_R, \qquad (10)$$

where n is the number of lung nodules.

3. RESULTS AND DISCUSSIONS

(8)

The segmentation results for solitary and juxtapleural nodules are shown in Fig. 4 and Fig. 5, respectively. Bilateral filtering replaces the pixel values of the image with a weighted average of similar and nearby pixel values, as shown in Fig. 4 (b) and Fig. 5 (b). Bit-plane slicing converts (9) ray levels of the image to values from 0 to 25 ping the value of pixels ranging from 0 to 127 to one

(a)   (b)   (c)   (d)   (e)
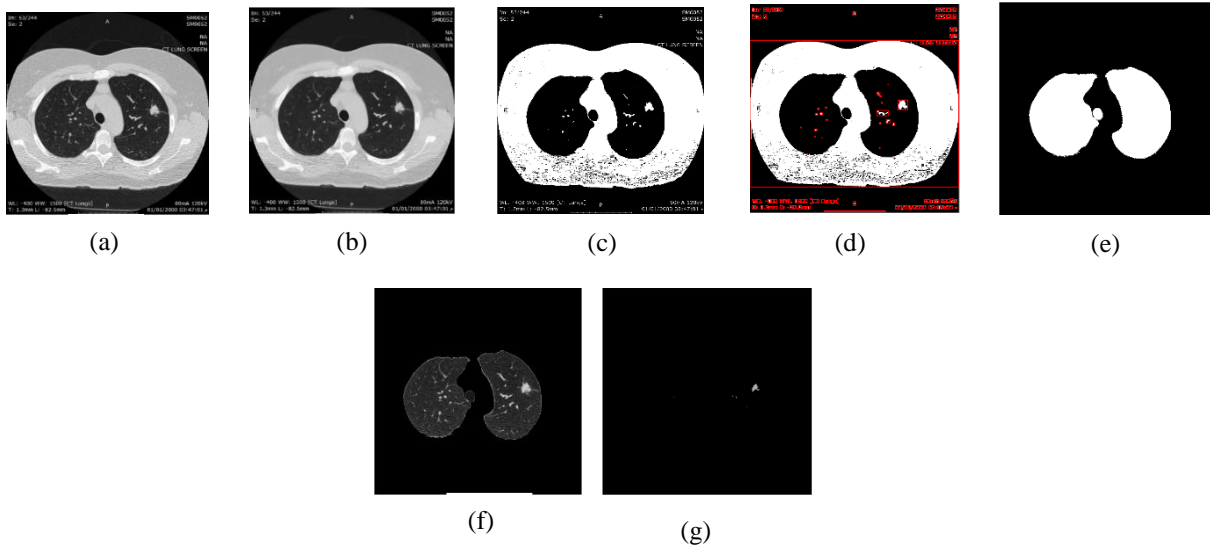
(f)   (g)

Figure 4: Segmentation of CT image with solitary nodule
(a): CT image with solitary nodule; (b): following bilateral filtering of a; (c): bit plane slicing of b; (d): bounding box use with c; (e): thresholding, lung border clearing, background removal, and filling the lung of d; (f): superimposed image; and (g): candidate nodules after using maximum intensity projection.
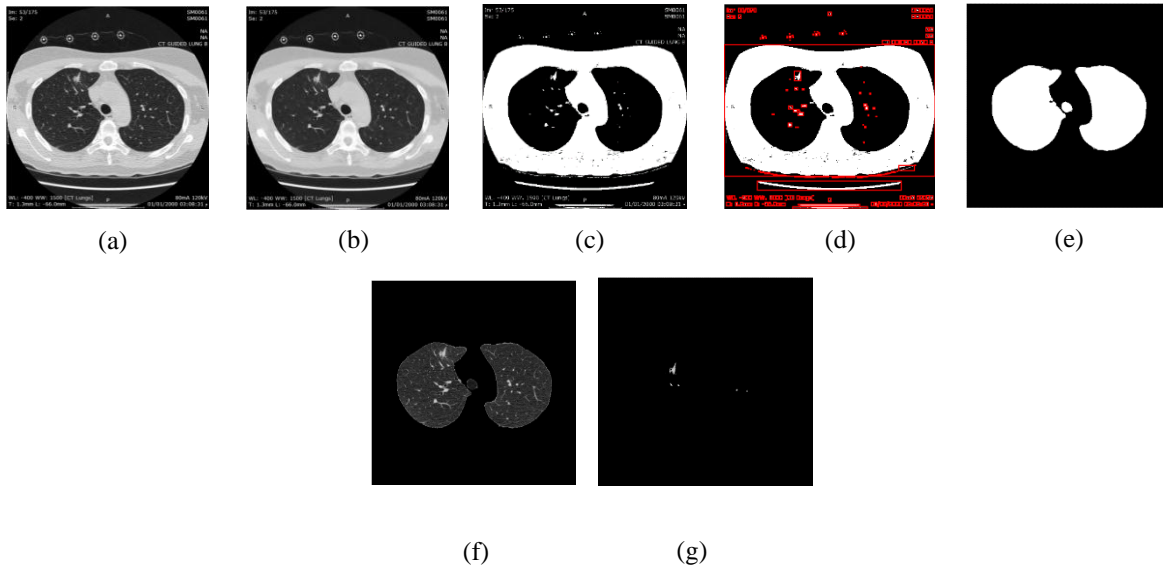
(a)   (b)   (c)   (d)   (e)

(f)   (g)

Figure 5: Segmentation of CT image with juxtapleural nodule
(a): CT image with juxtapleural nodule; (b): following bilateral filtering of a; (c) bit plane slicing of b; (d): bounding box use with c; (e): thresholding, lung border clearing, background removal, and filling the lung of d; (f): superimposed image; and (g): candidate nodules after using maximum intensity projection.

level (e.g. 0) and all the pixel values above 127 to another level (e.g. 1). This results in the transformation of the gray image into a binary image, as shown in Fig. 4 (c) and Fig. 5 (c). The bounding box specifies the image properties by creating a small rectangle (bounding box) that surrounds all the regions containing 1s. The thresholding technique is used to isolate the two lungs easily by mapping all the zero-valued pixels to ones and vice versa, as shown in Fig. 4 (d) and Fig. 5 (d). Border artifacts are removed by clearing the lung border, erosion, dilation and superimposing, as shown in Fig. 4 (e, f) and Fig. 5 (e, f). MIP evaluates the voxel projection with the highest attenuation value on every slice throughout the volume of a 2D image. Only the pixel with the highest Hounsfield number along the Z-axis is projected containing all dense structures (nodules) in a given volume. A morphologically close operation is performed after MIP using a structuring element (with a size of two pixels) that easily detects lung nodules, as shown in Fig. 4 (g) and Fig. 5 (g). The first step of the 3D reconstruction was extracting the 2D lung nodule features, which has been determined to aid in distinguishing the nodules from blood vessels in the 2D slice as shown in **Fig. 6**. Extraction of 2D lung nodule features is faster than extraction of 3D features. All candidate nodules (**Fig. 6 (a)**) are shown as blobs (**Fig 6 (b)**), which were then labelled and numbered from bottom to top and from left to right

(**Fig. 6 (c)**). Then, the texture and shape features were extracted for each blob. According to the extracted features, the rule-based classifier extracts the 2D nodules (**Fig. 6 (d)**). The X and Y centroids were measured to determine the location of the nodule. Each candidate nodule that had a diameter smaller than 3 mm or greater than 30 mm was excluded, which is the range of small nodules. For elliptical nodules, the eccentricity is close to 0. In addition, the roundness assisted in extracting the circular objects when these were equal to or less than 1 for objects that depart from circularity. Measuring the density of the nodule was performed with the solidity feature. This equals 1 for solid objects, as the nodules were denser than the surrounding lung region. Generally, the nodules have high gray-level contrast compared to blood vessels. The gray-level distribution of the CT image ranges from 0 to 255. So a gray-level histograms for the CT images is plotted to find the best threshold between the nodule and other tissues in the CT image. According to the plotted histograms for our CT images, the threshold between the nodule and the lung tissues was 150. So, a candidate nodule with a gray level below 200 was excluded, as (see **Fig. 7**). If another threshold is selected (for example, 150), gray levels below 150 will be excluded. In this case, all gray levels above 150 will be displayed and reconstructed as shown in **Fig**. 11(a), which is not desirable.

3D reconstruction is applied on 12 digital scan images of solitary and juxtapleural nodules, as there were two cases of segmentation failure in which the images have nodule and blood vessels (Fig. 11 (a)). Thus, 12 cases were reconstructed in 3D via SR. Surfaces were generated from extracted regions with the same intensity (similar voxel values). Fig. 8 shows a sample 3D lung model containing all slices of the CT image after extraction of the lung region as visualized on Slicer 4.8.1. 3D reconstruction for the extracted nodules was performed by reconstructing a specific slice where a tumor appeared with an equivalent diameter between 3 and 30 mm. According to the size of the nodules, the number of slices ranging from 4 to 38 slices was recorded. For example, **Fig. 9** (a, b and c) shows the CT image with candidate nodules including a solitary nodule. **Fig. 9 (d)** shows the resulting image from the MIP and BB algorithms**.** The rule-based classifier extracted the solitary nodule that appeared on 16 slices (**Fig. 9 (e)**) and then used SR to reconstruct the 3D nodule **(Fig. 9 (f)) for Case # 2 in Table 1**. The equivalent diameter of the 3D nodule was estimated to be 20.2 mm, with a location estimated at the centroid X = 350.0 and Y = 198.0, as visualized on the 3D Slicer (**Fig. 9 (g)**). Fig. 10 shows multiple solitary and juxtapleural nodules with different volumes. Fig. 10 (a, b, c, d, e and f) shows 3D nodules for Cases # (1, 3, 10, 5, 6 and 12) respectively in Table 1.

To evaluate the proposed model, the 3D estimated nodule volume was compared with the actual volume (V_A) of the nodule in the LIDC dataset. This method of evaluation produced a favorable result when applied to our dataset, whereas another method such as the Jaccard index (which measures the similarity between finite-sample sets) may not be suitable for our dataset. It is more specific for performance measures of large datasets with false-positive reduction techniques such as support vector machines and artificial neural networks which need more data for training and testing. Table 1 shows the results of the accuracy rates of the nodule estimated volumes obtained using the 3D algorithm.

The average accuracy rate of the 3D reconstruction algorithm for the 12 cases was 97.34 % while the average error rate was 2.66 %. With regard to 3D reconstruction, the extraction of texture and shape features for each blob in the 2D image via the rule-based classifier had a number of challenges, including:

- Several candidate nodules (blood vessels) with diameters between 3 and 30 mm were considered as nodules and they are extracted together with the true nodules. Therefore, other features such as roundness and eccentricity also needed to be extracted.
- Elliptical nodules have an eccentricity close to 0 and that of blood vessels is close to 1.
- Roundness helped reject blood vessels as these were more circular than nodules, and this value was relatively insensitive to irregular boundaries. However, several nodules appeared more circular. Therefore, they were rejected with the blood vessels.
- The solidity features were calculated for the candidate nodules. This feature reached 1 for the blood vessels. If the nodule had a regular boundary, it will therefore be rejected with the blood vessels.
- Each candidate nodule with a gray level below 200 was excluded as the threshold between the nodule and the lung tissues was 150 based on the lung gray-level histogram.
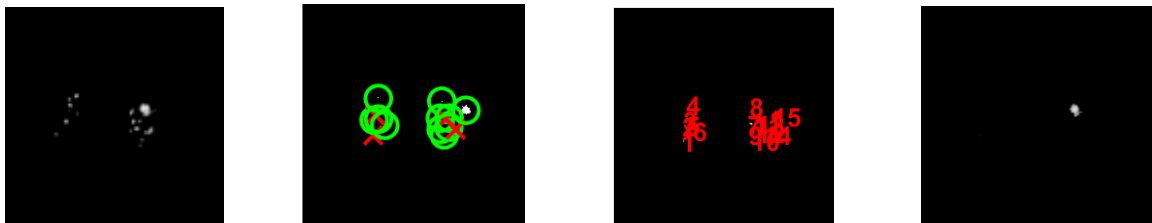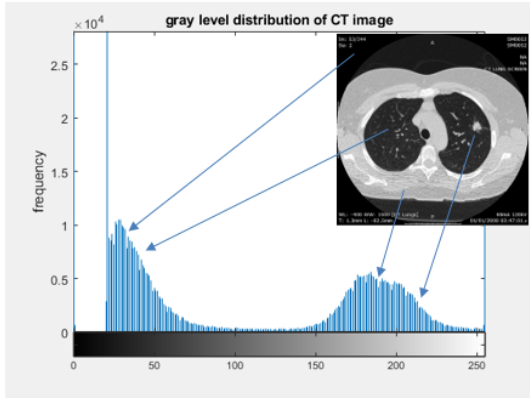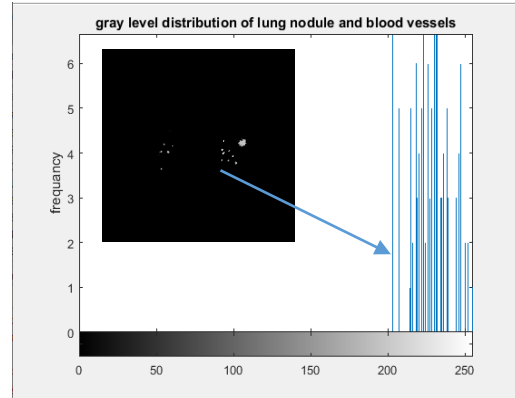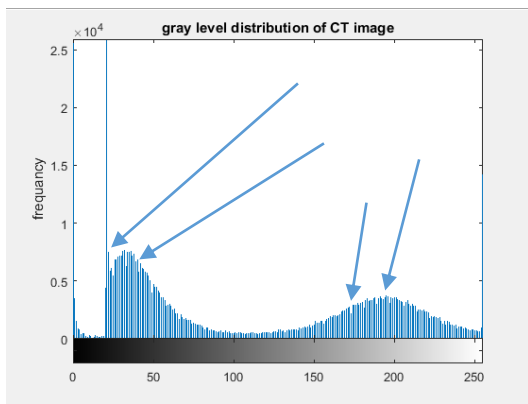

Figure 6: (a) Candidate nodules; (b) candidate nodules with blobs; (c) labeled and numbered candidate nodules; (d) extracted nodule.
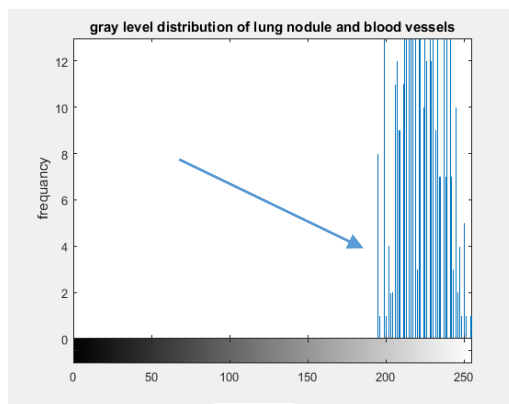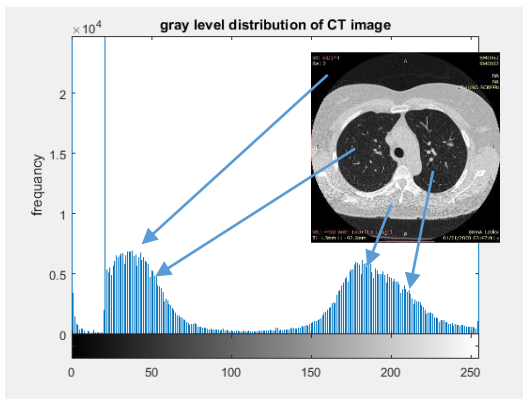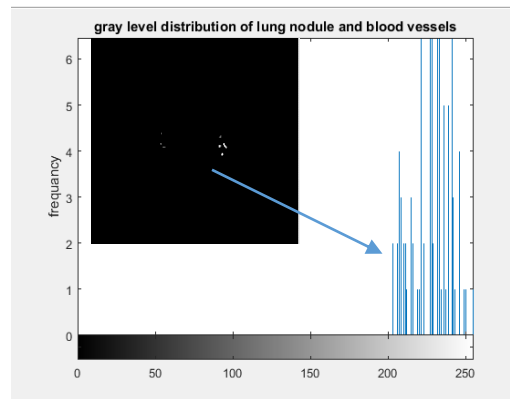
(a)

(b)

(c)

(d)

(e)

(f)

Figure 7: Gray-level distribution histograms
a, c and e: Gray-level distribution of different CT lung images
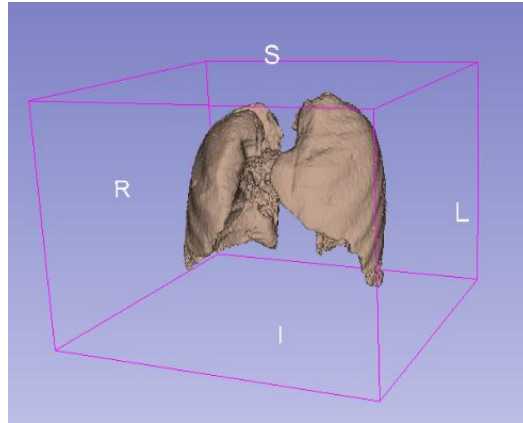b, d and f: Histograms of different candidate nodules

Figure 8: The 3D reconstructed lung

(a) (b) (c) (d) (e)

(f) (g)

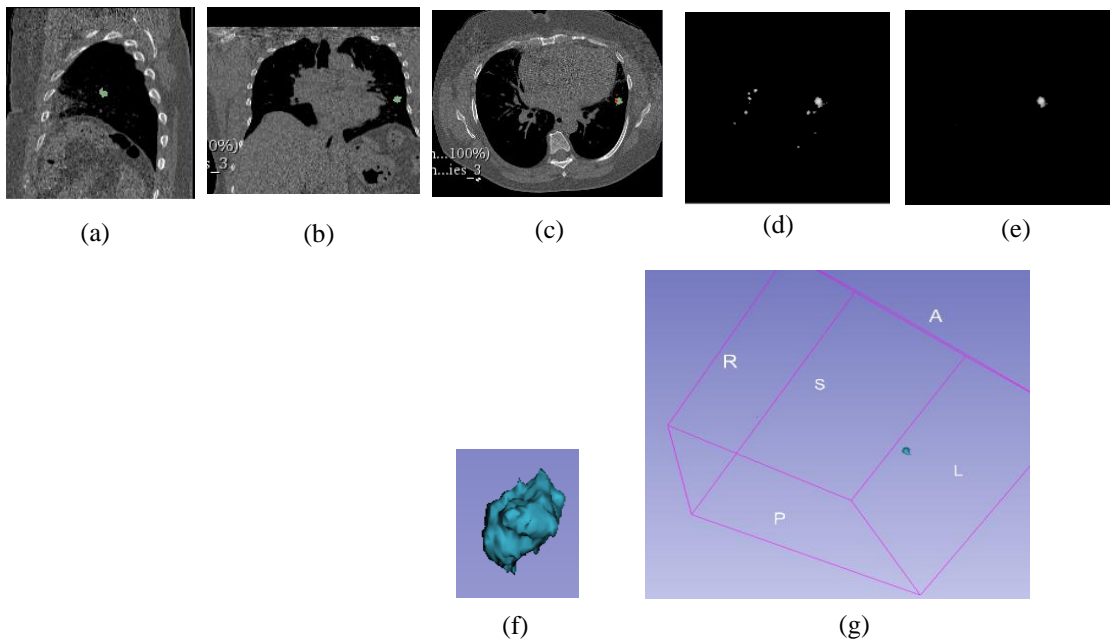**Figure 9: 3D reconstruction results on Solitary nodule**
a, b and c: The 2D CT image in three sections; d: resulting image from MIP and BB; e: resulting nodule after applying the rule-based classifier; f: zoom of the 3D reconstructed nodule after applying SR and 3D slicer with equivalent diameter = 20.2 mm; and g: the 3D reconstructed nodule located at centroid X = 350.0 and centroid Y = 198.0 inside the left lung.
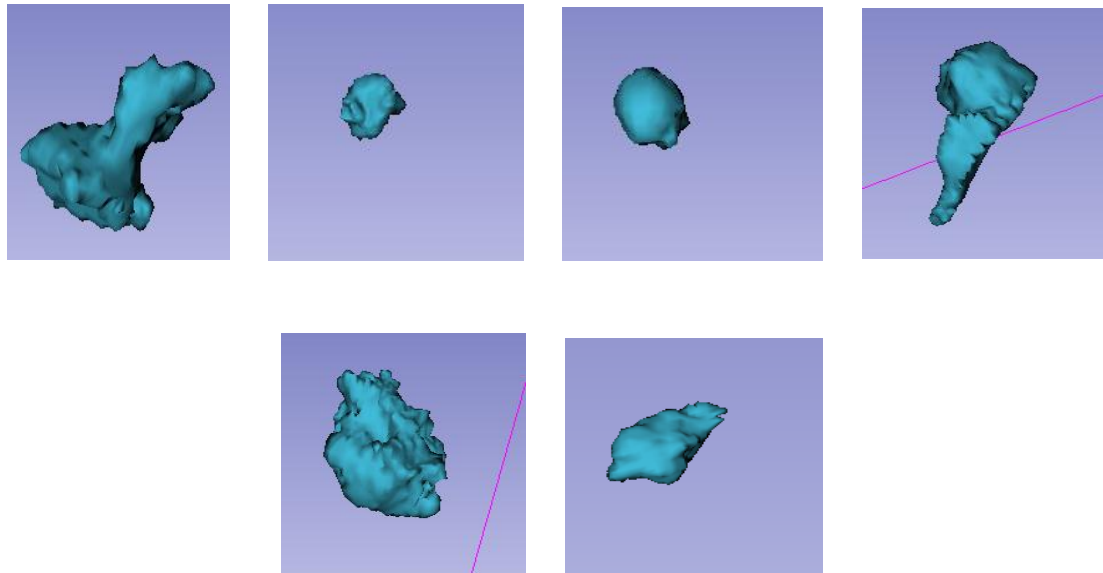
Figure 10: The 3D reconstruction results on multiple nodules (solitary and juxtapleural) with different volumes. a: Solitary nodule with equivalent diameter = 24.2 mm, centroid X = 230.0, and centroid Y = 200.0; b: solitary nodule with equivalent diameter = 3 mm, centroid X=383.3, and centroid Y = 189.0; c: solitary nodule with equivalent diameter = 6.8 mm, centroid X = 165.0, and centroid Y = 192.0; d: solitary nodule with equivalent diameter = 30 mm, centroid X = 195.0, and centroid Y = 202.0; e: juxtapleural nodule with equivalent diameter = 19.3 mm, centroid X = 166.0, and centroid Y = 175.0; and f: juxtapleural nodule with equivalent diameter = 12.7 mm, centroid X =372.0, and centroid Y = 111.0.

The rule-based classifier-based nodule extraction for 10 out of 14 cases. Two cases were segmented perfectly using the segmentation approach (bounding box + maximum intensity projection) without candidate nodules, whereas there were two cases of segmentation failure. Thus, 12 cases were reconstructed in 3D via SR as shown in **Fig. 11**. The 3D Slicer was interfaced with MATLAB to enhance the visualization of the SR as shown in **Fig. 10**. The volume of each nodule was then measured during evaluation. The 3D reconstruction model of pulmonary nodules produced a favorable result, as shown in Table 1, with minimum and maximum volume estimation accuracy rates of 94.956 % and 99.6627 %, respectively. The average accuracy rate and the average percentage error of the 3D reconstruction algorithm were 97.34 % and is 2.66 %, respectively.

Table 2 presents a comparison between the results of this current study and published studies. Our model exhibits the best results according to the LIDC dataset with different models for segmentation, reconstruction, and accuracy rates. Hina et al. [1]. Satya et al. [13] achieved an average error rate of 5.8% (overlap ratio difference) when applying fuzzy c-means clustering on only 10 nodules from 20 CT volumes. Ramyasri et al. [5] proposed K-means algorithm and 3D Slicer, but the dataset type either solitary or juxtapleural was not informed and

achieved an average error rate of 4.55% while, Prionjit et al. [10] achieved an accuracy of 95.68% when using thresholding and K-means clustering and applying an algorithm on 83 nodules. Zhipeng et al. [34] used a random walk algorithm to segment the lung nodules and volume vocal direction ternary pattern to extract pulmonary nodule texture features. The accuracy, sensitivity and specificity of the proposed method : 82.2%, 85.7%, and 78.8%, respectively. Our model achieved an average accuracy of 97.34% and average error rate of 2.66 % when applied on the LIDC dataset images. Thresholding, maximum intensity projection, bounding box, image intensity histogram and SR + 3D Slicer are applied. Our method showed promising results when compared to Hina et al. [1] who achieved an accuracy rate of 95% by using a mean-intensity-based threshold, image intensity histogram, and 3D Slicer application on the LIDC dataset images.

4. CONCLUSIONS
In this study, a robust 3D reconstruction algorithm for pulmonary nodules from 2D CT images was presented. The screening of a 3D nodule can support surgery planning. A segmentation and enhancement approach (bounding box + MIP) was applied. Extracting the lung nodule from the 2D candidate masses was performed features. SR was used for 3D reconstruction, and a 3D Slicer was used to visualize

the 3D lung nodules. Via rule-based classifier using shape and texture Nodule volumes and locations were estimated. The average accuracy and error rates of the 3D reconstruction algorithm were calculated. We demonstrated that our algorithm outperforms the previous state-of-the-art techniques in terms of segmentation (bounding box + MIP) and is significantly robust for two nodule types (solitary and juxtapleural), suggesting the suitability of our method for 3D implementation to minimize the radiologist effort through the automatic estimation of the VOI and

to enhance the accuracy of segmentation. Although the model showed some promising results in the reconstruction of the pulmonary nodules, further improvements could be achieved by including extra features such as elongation to extract the blood vessels and bronchioles and using a visualization toolkit for volume rendering rather than surface rendering. Also, diagnosis of lung cancer as benign or malignant can be achieved as a future work depending on the 3D nodule volume.
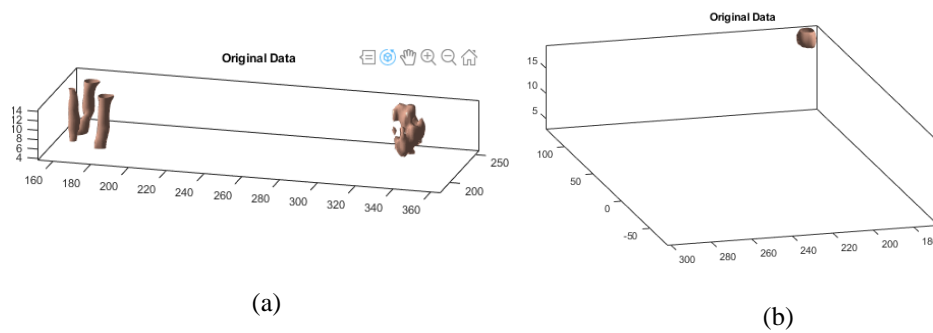

(a)

(b)

Figure 11: Visualization of 3D nodules and blood vessels by SR in Matlab

    (a)   3D Visualization with a gray-level threshold of 150
    (b)   3D Visualization with a gray-level threshold of 200

Table 1: Results of 3D algorithm showing the accuracy rate and percentage error of the estimated nodule volume

1	1287.59	1314	26.41	2.0511	97.95
2	881.9	895	13.1	1.485	98.515
3	14.3	15	0.7	4.895	95.105
4	4313.526	4405	91.474	2.121	97.8794
5	14130	14350	220	1.557	98.443
6	664.758	667	2.242	0.3373	99.6627
7	3762.273	38708	107.727	2.8633	97.1367
8	1071.987	1083	11.013	1.0273	98.973
9	2853.096	2997	143.904	5.0438	94.956
10	246.44	254.5	8.06	3.2706	96.7294
11	5201.08	5337	135.92	2.6133	97.3867
12	434.67	455	20.33	4.677	95.3229
Average	2905.135	5873.38	65.07	2.66	97.34

Table 2: Comparisons with published studies

١٣

#	Study	Techniques	Performance measure%	
			Average acc. %	**Average error rate %**
1	The presented work	MIP+BB and Surface rendering + 3D slicer	97.34	2.66
2	Hina et al. [1]	Mean intensity based threshold, image intensity histogram 3D slicer	95	NI
3	Satya et al. [13]	Fuzzy-c-means clustering	NI	5.8
4	Nandish et al. [5]	K-means algorithm 3D slicer	NI	4.55
5	Prionjit et al. [10]	Thresholding, k-means clustering and tumor nodule metastasis classification	95.68	NI
6	Zhipeng et al. [34]	Random walk algorithm and volume vocal direction ternary pattern	82.2	NI

NA**:** Not Available

Compliance with Ethical Standards:
- No funding was received to assist with the preparation of this manuscript.
- Conflict of Interest: Authors declare they have no conflict of interest.
- Ethical approval: No animal case was involved.
- Ethical approval: All procedures performed in studies involving human
- Ethical approval: This article does not contain any studies with human participants performed by any of the authors.
- Ethical approval: This article does not contain any studies with animals performed by any of the authors.

REFERENCES

[1] Hina Shakir, Tariq Mairaj Rasool Rasool Khan, and Haroon Rasheed (2018) 3-D segmentation of lung nodules using hybrid level sets. Computers in Biology and Medicine 96: 214-226.

[2] Macedo Firmino, Giovani Angelo, Higor Morais, Marcel R. Dantas, and Ricardo Valentim (2016) Computer-aided detection (CADe) and diagnosis (CADx) system for lung cancer with likelihood of malignancy. BioMedical Engineering Online 15: 1- 2.

[3] J. K. Field, S. W. Duffy, D. R. Baldwin, D K Whynes , A Devaraj , K E Brain , T Eisen , J Gosney , B A Green , J A Holemans , T Kavanagh , K M Kerr , M Ledson , K J Lifford , F E McRonald , A Nair , R D Page , M K B Parmar , D M Rassl , R C Rintoul , N J Screaton , N J Wald , D Weller , P R Williamson , G Yadegarfar and D M Hansell (2016) UK lung cancer RCT pilot screening trial: Baseline findings from the screening arm provide evidence for the potential implementation of lung cancer screening. Thorax 71: 161-170.

[4] Nanda Horeweg, Ernst Th Scholten, Pim A. de Jong (2014) Detection of lung cancer through low-dose CT screening (nelson): A prespecified analysis of screening test performance and interval cancers. The Lancet. Oncology 15: 1342-1350.

[5] Nandish S. Ramyasri Nayak and Prakashini Koteshwara (2018) Volume estimation of pulmonary lesion using chest CT sequence. International Journal of Engineering and Technology 7: 186-190.

[6] Diego M. Peña, S. Luo, and A. M. S. Abdelgader (2016) Auto diagnostics of lung nodules using minimal characteristics extraction technique. Diagnostics 6: 13.

[7] Jinke Wang and Haoyan Guo (2016) Automatic approach for lung segmentation with juxta-pleural nodules from thoracic CT based on contour tracing and correction. Computational and Mathematical Methods in Medicine 3: 1-13.

[8] Kan Chen, Bin Li, Lian-Fang Tian, Wen-Bo Zhu, and Ying-Han Bao (2014) Fuzzy speed function based active contour model for segmentation of pulmonary nodules in Frontiers in Bio-Medical Materials and Engineering. Proceedings of the 2nd international conference on Biomedical Engineering and Biotechnology 24: 539-547.

[9] Bin Li, Qing Lin Chen, Guangming Peng, Yuanxing Guo, Kan Chen, LianFang Tian, Shanxing Ou, and Lifei Wang (2016) Segmentation of pulmonary nodules using adaptive local region energy with probability density function-based similarity distance and multi-features clustering. BioMedical Engineering OnLine 15: 49.

[10] Prionjit Sarker, Md. Maruf, Hossain Shuvo, Zakir Hossain, and Sabbir Hasan (2017) Segmentation and classification of lung tumor from 3D CT image using K-means clustering algorithm. Proceedings of the 2017 4th international conference on Advances in Electrical Engineering (ICAEE), 28-30 September.

[11] Ming Yang, Senthil Periaswam, and Ying Wu (2007) false positive reduction in lung GGO nodule detection with 3D volume shape descriptor. IEEE Int conference on Acoustics, speech and signal processing 1:437-440.

[12] Serhat Ozekes, Onur Osman, and Osman N. Ucan (2008) Nodule detection in a lung region that's segmented with using genetic cellular neural networks and 3D template matching with fuzzy rule based thresholding," Korean Journal of Radiology 9: 1-9.

[13] Satya Prakash Sahu and Priyanka Agrawal, Narendra D Londhe and ShrishVerma (2017) A new hybrid approach using fuzzy clustering and morphological operations for lung segmentation in thoracic CT images. Biomedical and Pharmacology Journal 10: 1949-1961.

[14] William J. Kostis, Anthony P. Reeves, David F. Yankelevitz, and Claudia I. Henschke (2003) Three-Dimensional Segmentation and Growth-Rate Estimation of Small Pulmonary Nodules in Helical CT Images. IEEE Transactions on Medical Imaging 22:10.

[15] Stefano Diciotti; Giulia Picozzi; Massimo Falchini; Mario Mascalchi; Natale Villari; Guido Valli (2008) 3-D Segmentation Algorithm of Small Lung Nodules in Spiral CT Images. IEEE Transactions on Information Technology in Biomedicine 12:1.

[16] Jamshid Dehmeshki, Hamdan Amin, Manlio Valdivieso and Xujiong Ye (2008) Segmentation of Pulmonary Nodules in Thoracic CT Scans: A Region

Growing Approach. IEEE Transactions on Medical Imaging 27:4:467 – 480.

[17] Lung Cancer Database (2020), Available at https://www.cancerimagingarchive.net/. Accessed 11 Nov. 2020

[18] Ayat Karrar, Mai S. Mabrouk, and Manal Abdel Wahed (2020) Diagnosis of lung nodules from 2D computer tomography scans. Biomedical Engineering – Applications, Basis and Communications 32: 2.

[19] Sweety Deswal, Shailender Gupta, and Bharat Bhushan (2015) A survey of various bilateral filtering techniques. Int J Sig Pro 8: 105-120.

[20] Haibo Gao, Wenjuan Zeng, and Jifeng Chen (2019) An improved gray-scale transformation method for pseudo-color image enhancement. Computer Optics 43:78-82.

[21] Zhuofu Deng, Binbin Wang, and Zhiliang Zhu (2020) BE-FNet: 3D bounding box estimation feature pyramid network for accurate and efficient maxillary sinus segmentation. Mathematical Problems in Engineering 2020:1-16.

[22] Lukas Ebner, Justus E. Roos, Jared D. Christensen, Tomas Dobrocky, Lars Leidolt, Barbara Brela, Verena C. Obmann, Sonya Joy, Adrian Huber, and Andreas Christe (2016) Maximum-intensity-projection and computer-aided-detection algorithms as stand-alone reader devices in lung cancer screening using different dose levels and reconstruction kernels. AJR. American Journal of Roentgenology 207:282-288.

[23] Toyofumi F. Chen-Yoshikawa and Hiroshi Date (2016) Update on three-dimensional image reconstruction for preoperative simulation in thoracic surgery. Journal of Thoracic Disease 8: 295-301.

[24] Jiaxin Wen, Xiaobin Hou, Xiangyang Chu, Xinying Xue, and Zhiqiang Xue (2015) Application of three dimensional reconstruction technique in selection of incision of thoracic surgical operation with robot. International Journal of Clinical and Experimental Medicine 8: 17818-17823.

[25] Qingjie Yang, Baiyi Xie, Meng Hu, Xiaoyan Sun, Xiaoyang Huang, and Ming Guo (2016) Thoracoscopic anatomic pulmonary segmentectomy: A 3-dimensional guided imaging system for lung operations, Interactive Cardiovascular

[26] Hadia Bashir, Fawad Hussain, and Muhammad Haroon Yousaf (2015) Smart algorithm for 3D reconstruction and segmentation of brain tumor from MRIs using slice selection mechanism. Smart Computing Review 5: 3.

[27] Jibi John and Mini M.G. (2016) Multilevel thresholding based segmentation and feature extraction for pulmonary nodule detection. Procedia Technology 24:957-963.

[28] Noor Khehrah, Muhammad Shahid Farid, Saira Bilal, and Muhammad Hassan Khan (2020) Lung nodule detection in CT images using statistical and shape-based features. Journal of Imaging 6:2.

[29] Mehdi Alilou, Niha Beig, Mahdi Orooji (2017) An integrated segmentation and shape-based classification scheme for distinguishing adenocarcinomas from granulomas on lung CT. Medical Physics 44:3556-3569.

[30] Kikinis, Ron, and Steve Pieper (2012) 3D Slicer as a tool for interactive brain lesion segmentation. International Journal of Medical Imaging and Technology 2:6982-6984.

[31] Csaba Pinter, Andras Lasso, An Wang, Gregory C. Sharp, Kevin Alexander, David Jaffray, and Gabor Fichtinger (2015) Performing radiation therapy research using the open-source SlicerRT toolkit," IFMBE Proceedings, World Congress on Medical Physics and Biomedical Engineering (book). Toronto, Canada, pp 622-625.

[32] Anna Rita Larici, Alessandra Farchione, Paola Franchi, Mario Ciliberto, Giuseppe Cicchetti, Lucio Calandriello, Annemilia del Ciello and Lorenzo Bonomo (2017) "Lung nodules: size still matters", Eur Respir Rev: 26.

[33] Sarah Soltaninejad, Mohsen Keshani, and Farshad Tajeripour (2012) Lung Nodule Detection by KNN Classifier and Active Contour Modelling and 3D Visualization. The 16th CSI International Symposium on Artificial Intelligence and Signal Processing.

[34] Zhipeng Fan, Huadong Sun, Cong Ren, Xiaowei Han & Zhijie Zhao (2020) Texture recognition of pulmonary nodules based on volume local direction ternary pattern. Bioengineered 11: 904-920.